

FWI using reflections for deep velocity model updates

Yang Yang*, Jaime Ramos-Martinez, Normal Daniel Whitmore, Alejandro A. Valenciano, Guanghui Huang, and Nizar Chemingui, PGS

Summary

Full Waveform Inversion (FWI) utilizes refractions and reflections to improve the accuracy and resolution of the earth subsurface models. The use of refractions is limited by the maximum offset of the acquisition, up to their maximum penetration depth. In contrast, reflections can produce deeper updates with small offsets, but they demand robust and more sophisticated algorithms.

FWI using reflections needs hard boundaries in the velocity/density models to simulate backscatter energy and generate the velocity sensitivity kernels. Alternatively, one can apply the wave-equation and first-order Born approximation to decompose the seismic wavefields into background and perturbations. Here, we utilize the acoustic wave-equation in terms of vector reflectivity to produce reflections in the modeling engine of FWI. The vector reflectivity wave-equation is derived by parametrizing the variable density acoustic wave-equation. The main advantages of its insertion in the FWI algorithm are the following: it does not require the construction of density/hard boundaries in the velocity model to generate reflections; it allows the use of reflected events without the need of solving two different wave-equations in the forward and backward propagation; it is more accurate than the method based on the first-order Born approximation and perturbation theory. We illustrate with synthetic and field data examples the use of deep reflections to produce FWI updates.

Introduction

In the early stages of a model-building project, FWI relies mostly on refracted events since they are easier to generate and utilize. However, refractions can only update the velocity model up to their maximum penetration depth. Consequently, the need for deep updates has triggered a demand for long offset acquisitions in modern seismic surveys. As an alternative to long offsets, one can use reflection data for deep model updating. Reflections, on the other hand, demand robust and sophisticated inversions, beyond conventional algorithms.

Excluding the high wavenumbers when updating the long-wavelength components of the velocity model is a critical ingredient of a reflection-based FWI. There are different strategies to separate the low- from the high-wavenumber components of the velocity updates. The most common industry approach, Born approximation and perturbation theory, involves the cascade of two different solutions to the

acoustic wave-equation (Mora, 1989). However, this is an approximate solution that doubles the computational costs. In 2016, Ramos-Martinez et al. proposed a robust FWI solution based on a velocity gradient derived using inverse scattering theory (ISIC). Combined with a variable density wave-equation, the ISIC-based FWI gradient removes the migration isochrones. It produces clean low-wavenumber updates at the cost of only one-pass of the wave-equation.

Here, we propose a new efficient FWI workflow for refractions and reflections based on the acoustic wave-equation with velocity and reflectivity as parameters (Whitmore et al., 2020). The new modeling engine does not require the construction of a density model to simulate the scattered events and provides the full forward and backward wavefield in one modeling realization. The separation of low- and high-wavenumber components in the gradient is performed using the method outlined by Ramos-Martinez et al. (2016). First, we show the derivation of the wave-equation in terms of velocity and reflectivity. Then we illustrate how to use it in combination with the velocity sensitivity kernel to separate the wavenumber components in FWI. Finally, we demonstrate the performance of the proposed workflow using synthetic and field data examples.

Method

The variable density acoustic wave-equation is written as:

$$\frac{1}{V(\mathbf{x})^2} \frac{\partial^2 P(\mathbf{x}, t)}{\partial t^2} - \rho(\mathbf{x}) \nabla \cdot \left(\frac{1}{\rho(\mathbf{x})} \nabla P(\mathbf{x}, t) \right) = S(\mathbf{x}, t), \quad (1)$$

where P is the complete pressure wavefield which is a function of space (\mathbf{x}) and time (t), V is the velocity, ρ is the density and S is the source. Using the definition of acoustic impedance ($Z(\mathbf{x}) = \rho(\mathbf{x})V(\mathbf{x})$), and performing a change of variable from impedance to reflectivity, equation (1) can be written as:

$$\frac{1}{V(\mathbf{x})^2} \frac{\partial^2 P(\mathbf{x}, t)}{\partial t^2} - \nabla^2 P(\mathbf{x}, t) - \frac{\nabla V(\mathbf{x})}{V(\mathbf{x})} \cdot \nabla P(\mathbf{x}, t) + 2\mathbf{R}(\mathbf{x}) \cdot \nabla P(\mathbf{x}, t) = S(\mathbf{x}, t) \quad (2)$$

Here $\mathbf{R}(\mathbf{x}) = \frac{1}{2} \frac{\nabla Z(\mathbf{x})}{Z(\mathbf{x})}$ is the vector reflectivity (Sheriff and Geldart, 1995), which can be derived from the migration image. Note that for a smooth velocity model, the third term in equation (2) can be neglected, and the scattering will primarily be produced from the reflectivity term. For constant density, the last two terms on the left-hand side are

FWI using reflections for deep velocity model updates

zero, and the equation has the same form of the scalar wave-equation. Compared with Born modeling (Mora, 1989), the assumption of small velocity perturbation is not required and higher order scatterings are also considered. Also, note that only one wave-equation needs to be solved when compared with the two required equations by Born modeling.

To separate the low- (tomography term) from the high-wavenumber (migration term) components in the gradient, we use an efficient implementation of the velocity sensitivity kernel (Ramos-Martinez et al., 2016), which is defined as:

$$K_V(\mathbf{x}) = \frac{1}{2I(\mathbf{x})} \left[\int \left(W_1(\mathbf{x}, t) \frac{1}{V(\mathbf{x}, t)^2} \frac{\partial P(\mathbf{x}, t)}{\partial t} \frac{\partial Q(\mathbf{x}, t)}{\partial t} - W_2(\mathbf{x}, t) \nabla P(\mathbf{x}, t) \cdot \nabla Q(\mathbf{x}, t) \right) dt \right], \quad (3)$$

where W_1 , W_2 are dynamic weights, P and Q are the forward and adjoint wavefields and I is the illumination term.

Synthetic examples

First, we compute the velocity sensitivity kernel for a homogeneous layer overlaying a half-space by using equations 2 and 3 in the FWI and compare it with that calculated from the Born approximation. Figure 1 shows the results for both cases. Figure 1b shows the new FWI workflow produces rabbit ears with fewer artifacts near the reflector.

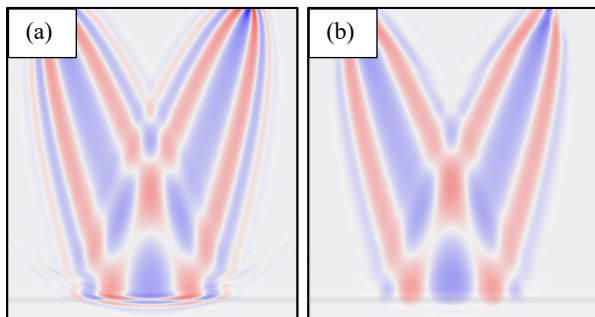


Figure 1: Rabbit ears from (a) Born modeling and from (b) the new reflectivity modeling engine and velocity sensitivity kernel. The background shows the migrated image used as input reflectivity in the modeling.

Next, we compared two different inversion strategies by using a modified 2D slice of the SEG Overthrust model with an extra water layer. We used a fixed-spread acquisition geometry consisting of 81 shots and 601 receivers that are evenly distributed at a constant depth of 10 m. The data contained no offsets beyond 4 km. The initial model (Figure 3b) was a heavily smoothed version of the exact model (Figure 3a). The initial reflectivity model was generated

from reverse time migration using the Inverse Scattering Imaging Condition (Whitmore and Crawley, 2012).

Figure 2 shows the synthetic shot gathers that illustrate the performance of the new reflectivity modeling engine. The frequency bandwidth for the modeling ranged from 3 Hz to 15 Hz. The reflectivity modeling method (Figure 2b) gives the same seismic response as the modeling with the variable velocity and density (Figure 2a). Figure 2d shows the Born modeled data, although kinematically correct, it shows some phase and amplitude differences with respect to Figures 2a and 2b. If constant density is used, and the velocity model does not present any contrasts, the reflections are not modeled (Figure 2c). By implementing Equation 2 as the FWI modeling engine, we demonstrate a way to generate reflections using the high-wavenumber reflectivity. The differences between the modeling and the field data are used to update the model's low-wavenumber content with FWI.

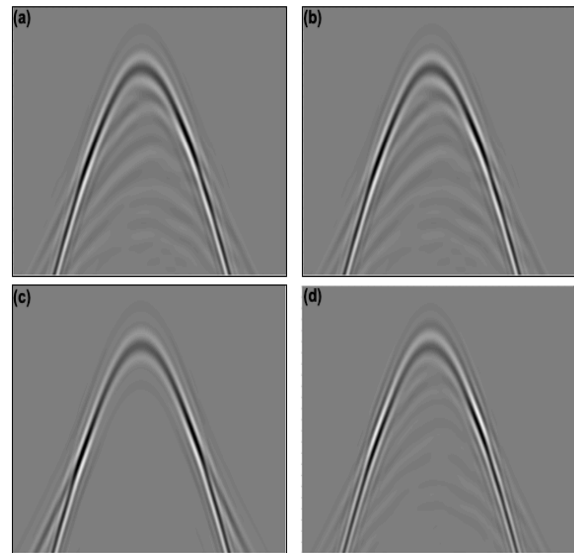


Figure 2: Synthetic shot gathers for the Overthrust model. (a) modeling using the variable density acoustic wave-equation (Equation 1). (b) Modeling using the wave-equation parameterized with velocity and reflectivity (Equation 2). (c) Velocity only modeling with the initial velocity model and constant density. (d) Born modeling with velocity and actual reflectivity.

The FWI results are shown in Figure 3. It used a maximum frequency of 7.5 Hz. The input data only had reflections. The new implementation improves the low-wavenumber content of the velocity field (Figure 3c). Note how the layers start to be delineated by the new FWI application. This model was then used as the input for a conventional inversion (cross-correlation gradient) to incorporate the high-wavenumber features of the model (Figure 3d). For comparison, we performed the inversion using FWI with a cross-correlation

FWI using reflections for deep velocity model updates

gradient from the starting (smooth) velocity model (Figure 3e). With the new cascaded FWI workflow, the background model is more accurate, and the high-wavenumber features are enhanced.

Deep FWI Updates in Canadian Orphan Basin

We illustrate the new FWI method using data from the Canadian Tablelands Orphan Basin. The data were acquired with multisensor streamers with offsets up to 8 km. The shallow part of the model used mostly updated with refracted waves in FWI. Following this, reflections were incorporated up to a maximum frequency of 25 Hz producing a high-resolution model. The thick water column (approximately 2 km), combined with an 8 km maximum offset made it challenging to use transmission driven FWI beyond the top Cretaceous (4 km depth).

The new FWI algorithm updated the velocity model beyond the maximum penetration of the refracted waves, resolving the model deeper than the top Cretaceous sequences (greater than 4 km of depth). Figure 4 shows the updates overlaid on the reflectivity model; in general, and as demonstrated in the migrated gathers (Figure 5a) there was a need to reduce the velocity. Note how, to the left of the model, the updates are restricted by the fault planes as yellow arrows indicate. To the right, they also conform to the geology. Figure 5 shows the common image gathers before and after the deep FWI updates. The initial gathers show some residual curvature (Figure 5a). After the deep FWI, the gathers are flatter (Figure 5b), especially for locations as indicated by yellow arrows.

Lastly, Figure 6 shows a depth slice at 5.6 km of the final reflectivity model (Figure 6a), the initial velocity model (Figure 6b), and the final FWI model (Figure 6c). The resulting velocity model clearly displays enhanced spatial resolution that is conformable to the structure.

Conclusions

We have presented a new FWI solution that uses both velocities and reflectivity to enable a simple, efficient, and more accurate model building workflow. The procedure is capable of simulating reflections without the need to either build a density model or rely on the first-order Born approximation to decompose the seismic wavefields. The new FWI presents a practical approach for deep model updating using reflection data.

Acknowledgments

We thank Tiago Alcantara and Mikhail Orlovich for their assistance in the field data example. We also thank PGS

multiclient for their permission to publish the field data results.

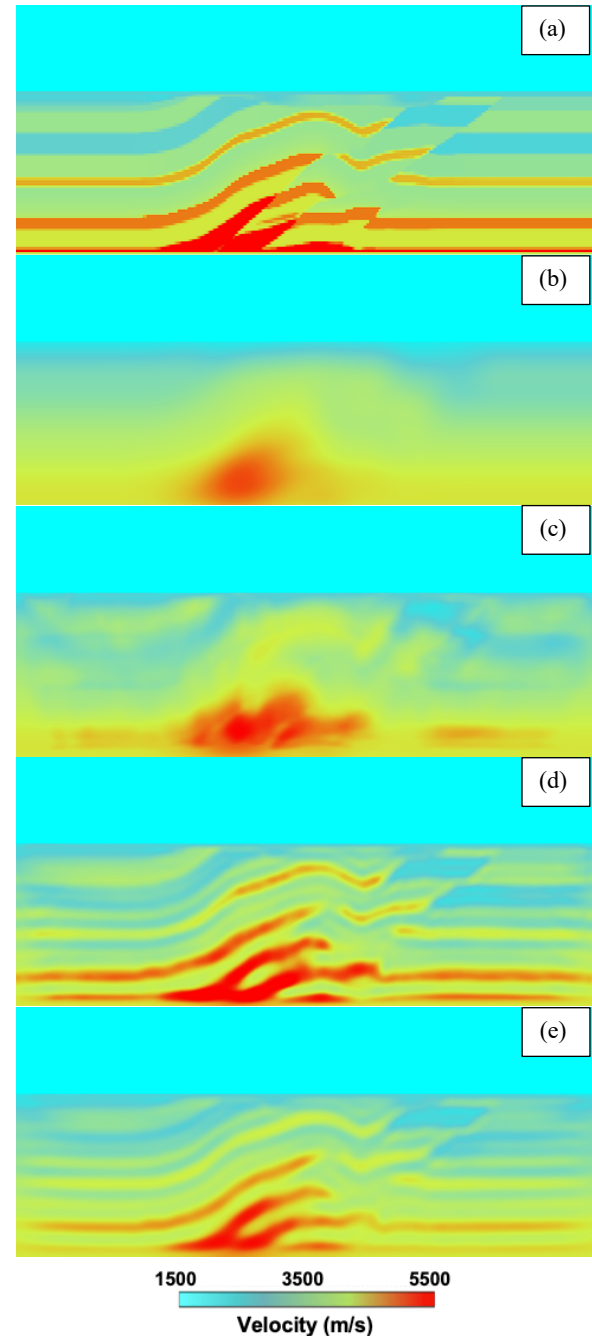


Figure 3: Overthrust model. (a) True velocity model. (b) Initial velocity model. (c) Our FWI model using reflectivity modelling. (d) FWI model using cross correlation gradient with (c) as the initial. (e) FWI model using cross correlation with (b) as the initial.

FWI using reflections for deep velocity model updates

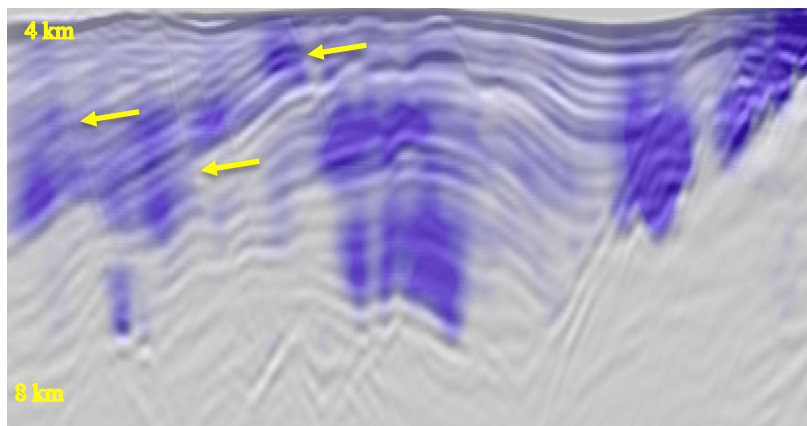


Figure 4: Deep FWI the updates overlaid on the reflectivity model, in general there was a need to reduce the velocity underneath the top Cretaceous (4km depth).

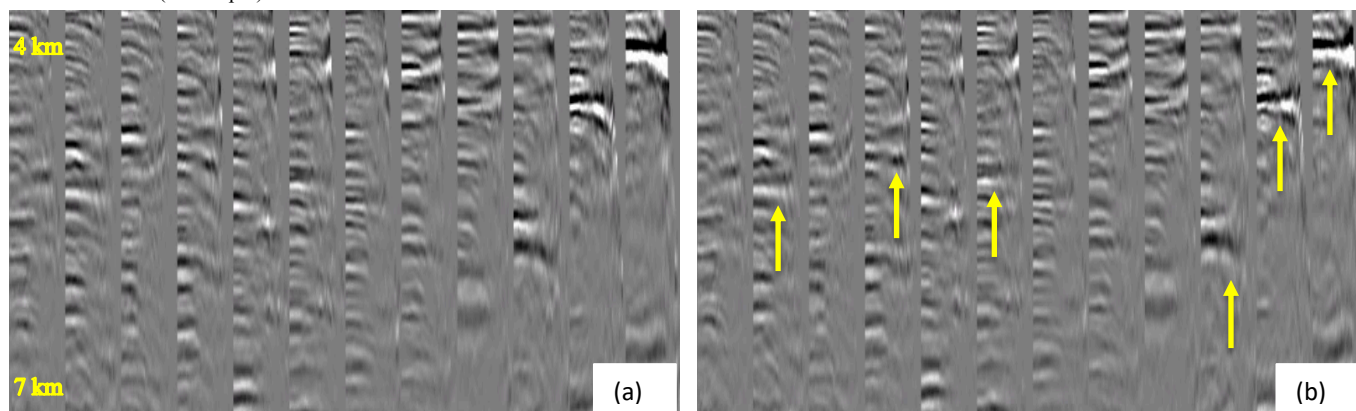


Figure 5: Common image gathers before and after the deep FWI updates. (a) The initial gathers show residual curvature. (b) After FWI, the gathers display less moveout.

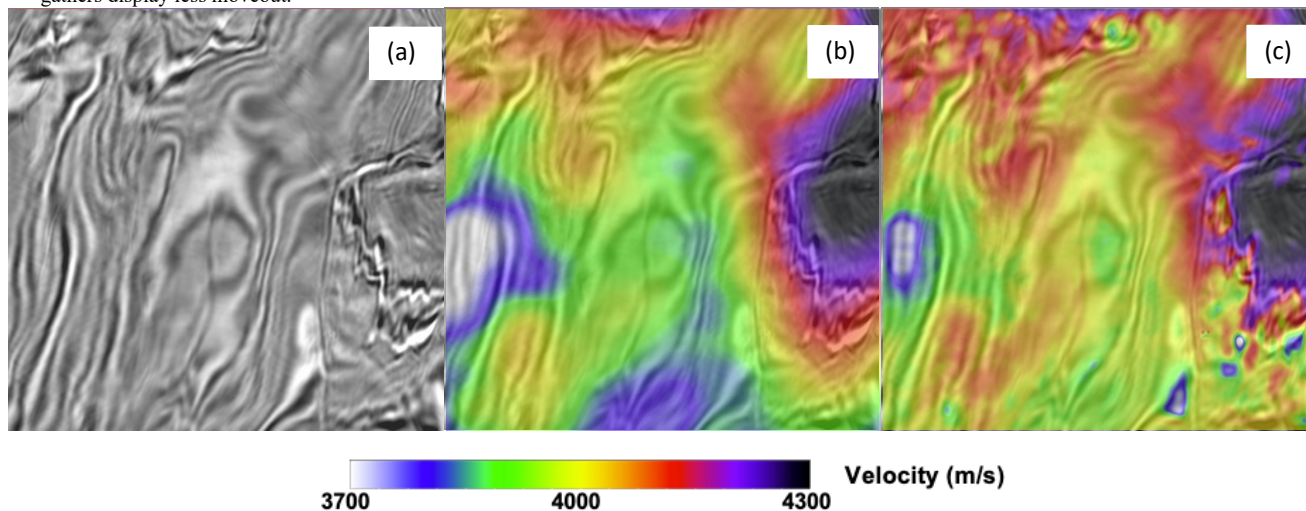


Figure 6: Depth slice at 5.6 km. (a) The final reflectivity model. (b) The initial velocity model. (c) The final FWI model. The FWI velocity model displays enhanced spatial resolution that is conformable to the structure.

REFERENCES

- Alkhalifah, T., 2014, Scattering-angle based filtering of the waveform inversion gradients: *Geophysical Journal International*, **200**, 363–373, doi: <https://doi.org/10.1093/gji/ggu379>.
- Frugier, E., T. Alcantara, and B. Viriout, 2020, High-resolution Full Waveform Inversion model building in deep-water environment: A case study in the Orphan basin: *GeoConvention*, accepted.
- Gomes, A., and N. Chazalnoel, 2017, Extending the reach of full-waveform inversion with reflection data: Potential and challenges: 87th Annual International Meeting, SEG, Expanded Abstracts, 1454–1459, doi: <https://doi.org/10.1190/segam2017-17731403.1>.
- Mora, P., 1989, Inversion = migration + tomography: *Geophysics*, **54**, 1575–1586, doi: <https://doi.org/10.1190/1.1442625>.
- Ramos-Martinez, J., S. Crawley, K. Zou, A. A. Valenciano, L. Qiu, and N. Chemingui, 2016, A robust gradient for long wavelength FWI updates: 78th Annual International Conference and Exhibition, EAGE, Extended Abstracts, doi: <https://doi.org/10.3997/2214-4609.201601536>.
- Sheriff, R. E., and L. P. Geldart, 1995, *Exploration seismology*, 2nd ed.: Cambridge University Press.
- Tarantola, A., 1984, Inversion of seismic reflection data in the acoustic approximation: *Geophysics*, **49**, 1259–1266, doi: <https://doi.org/10.1190/1.1441754>.
- Whitmore, N. D., and S. Crawley, 2012, Applications of RTM inverse scattering imaging conditions: 82nd Annual International Meeting, SEG, Expanded Abstracts, 1–6, doi: <https://doi.org/10.1190/segam2012-0779.1>.
- Whitmore, N. D., J. Ramos-Martinez, Y. Yang, and A. A. Valenciano, 2020, Full wavefield modeling with vector reflectivity: 82nd Annual International Conference and Exhibition, EAGE, Extended Abstracts, 1–5, doi: <https://doi.org/10.3997/2214-4609.202010332>.
- Xu, S., D. Wang, F. Chen, Y. Zhang, and G. Lambaré, 2012, Full waveform inversion for reflected seismic data: 74th Annual International Conference and Exhibition, EAGE, Extended Abstracts, W024, doi: <https://doi.org/10.3997/2214-4609.20148725>.
- Zhou, W., R. Brossier, S. Operto, and J. Virieux, 2015, Full waveform inversion of diving and reflected waves for velocity model building with impedance inversion based on scale separation: *Geophysical Journal International*, **202**, 1535–1554, doi: <https://doi.org/10.1093/gji/ggv228>.